

# Effect of Surface Unsteady Pressure Field on Global Beam Jitter for a Hemisphere-on-Cylinder Turret

Nicholas De Lucca<sup>1</sup>, Stanislav Gordeyev<sup>2</sup>, and Eric Jumper<sup>3</sup>  
*University of Notre Dame, Notre Dame, Indiana, 46545*

**Simultaneous point surface pressure measurements, accelerometer, optical wavefront and jitter measurements were performed using a hemisphere-on-cylinder turret with realistic geometric features like “smiles” at  $M = 0.33$  and  $M = 0.4$ . A Linear Stochastic Estimation (LSE) technique was used to separate the aero-optical and the aero-mechanical jitter components. The unsteady pressure field on the turret was approximated using a combination of LSE technique and Proper Orthogonal Decomposition. To determine the driving factors of the aero-optical jitter, correlations were performed between the global POD modes, local pressure sensors and the measured aero-optical jitter. To further investigate sources of aero-optical jitter, correlations were performed between dominant wavefront modes and the measured jitter. It was found that different flow features, primarily the unsteady separation line, wake vertical global motion and the vortical structures formed in the separated wake influence the aero-optical jitter, both indirectly via Biot-Savart induction mechanism and directly, when crossing the laser beam. It was also found that different flow features affect the aero-optical jitter at different frequency ranges. Total jitter reduction based on the LSE technique is discussed and possible expansion of the technique using surface pressure measurements is investigated.**

## I. Introduction

THE hemisphere-on-cylinder turret is a commonly-used geometry in directed energy or free-space communication systems, as it provides a large field-of-regard. For airborne directed energy applications, however, this turret geometry presents several aero-optical challenges, as the turret geometry produces a highly three-dimensional turbulent flow field [1]. This highly turbulent flow at flight speeds introduces compressible turbulent regions over the aperture of the turret, aberrating the laser beam. Aero-optical properties of hemisphere-on-cylinder turrets have been studied extensively in recent years in-flight on the AAOL [2,3] and through CFD [4,5,6].

One often overlooked optical issue introduced by the hemisphere-on-cylinder turret geometry is beam jitter, a global unsteady motion of the laser beam. Beam jitter adversely affects both directed energy and communication systems. At large ranges, even a few microradians of beam jitter can cause a system to miss a target entirely. For the communications systems, this can introduce signal dropouts, and for the directed energy systems it will increase the time needed to deposit sufficient energy on a target. As such, it is desirable to measure and predict the beam jitter so that it can be corrected or mitigated. There are two sources of beam jitter introduced by the flow in around turrets: aero-optical jitter introduced by turbulent structures of sizes comparable to the turret aperture and aero-mechanical jitter driven by an aero-elastic response of the turret to an unsteady pressure field acting on the turret [7]. The possibility to separate these two jitter components using the simultaneous jitter-accelerometer measurements has been previously demonstrated [7]. Additionally, the unsteady surface pressure fields and the resulted unsteady force applied to the turret geometry in-flight have been investigated using a pressure sensitive paint (PSP) [8,9,10].

The hemisphere-on-cylinder turret geometry creates several distinct flow features that combine into a highly three-dimensional flow field. This flow field is shown above in Figure 1. The flow on the upstream portion of the turret is dominated by a turbulent boundary layer. A necklace vortex forms around the base of the turret and extends downstream. The adverse pressure gradient of the downstream portion of the turret forces a separation to occur along a line that depends on the Reynolds number. This separated wake region is dominated by a recirculation

---

<sup>1</sup> Graduate Student, Department of Mechanical and Aerospace Engineering, Hessert Laboratory for Aerospace Research, Notre Dame, IN 46556, Student Member.

<sup>2</sup> Research Associate Professor, Department of Mechanical and Aerospace Engineering, Hessert Laboratory for Aerospace Research, Notre Dame, IN 46556, AIAA Associate Fellow.

<sup>3</sup> Professor, Department of Mechanical and Aerospace Engineering, Hessert Laboratory for Aerospace Research, Notre Dame, IN 46556, AIAA Fellow.

region with two horn vortices. If the turret has a flat window, a slope discontinuity around the window additionally trips the flow, and, depending on the viewing angle, a separation bubble will form over an upstream part of the window aperture [11].

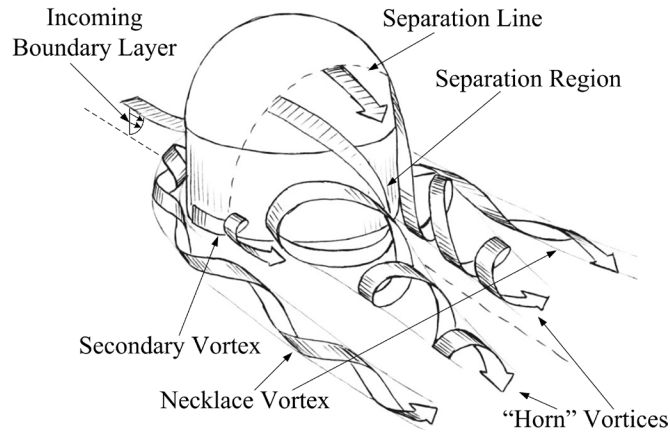


**Figure 1: Dominant flow structures around a hemisphere-on-cylinder turret.**

In this paper, simultaneous optical, pressure and accelerometer measurements are presented and analyzed for a hemisphere-on-cylinder turret with realistic “smile” cut-outs. The point pressure measurements were used to determine the effect of the turret “smiles” locations on the various turret flow features and directly correlated with the aero-optical jitter.

## II. Experimental Setup

The experiment was performed in the 3’x3’ Mach 0.6 White Field wind tunnel at the University of Notre Dame. The turret used was a replica of the AAOL turret, with a 12 inch diameter and a 4 inch aperture. A depiction of the turret is shown below in Figure 2, left. The turret has several realistic features including “smile” cut-outs (red arrow) and gaps (green arrow) between the rotating part of the turret and the trunnions. Data were acquired at  $M = 0.33$  and  $M = 0.4$ . The data were collected for the window azimuthal angles of  $0^\circ$  (facing upstream),  $90^\circ$  (facing sideways) and  $180^\circ$  (facing downstream) with a fixed elevation angle of  $45^\circ$ .

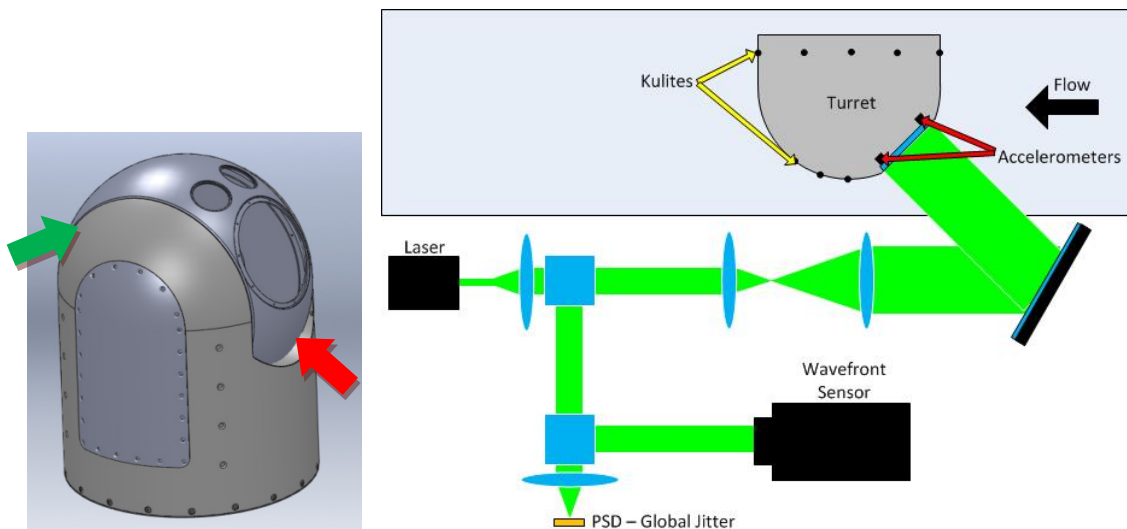


**Figure 2: Left: The turret assembly. The red arrow points to the “smile”, the green arrow indicates gaps. Right: The schematic of the experimental setup.**

Wavefront measurements were performed simultaneously with the pressure and accelerometer measurements. The instrumentation and optical set up is shown in Figure 2, right. Wavefronts were measured with a high-speed Shack-Hartmann wavefront sensor. The wavefronts were obtained at 20 kHz using 32x32 sub-apertures. A total of 46,000 frames were taken for each case, totaling 2.3 seconds. The global jitter of the beam was measured using a Position Sensing Device (PSD). Three one-axis and one three-axis accelerometers were placed on the rear side of the mirror assembly, with the three-axis accelerometer in the middle and the one-axis accelerometers equally spaced at the edges. To obtain the local pressure measurements, a total of 16 unsteady pressure sensors were used. The sensors used were from Kulite Inc, model XT-140-10D, 10 psi differential sensors. The pressure sensor locations are given in Figure 3. The turret had 26 possible locations for pressure sensors that were used in previous experiments [8,9,10], but, for various reasons, only a subset of 8 of those locations were used for this work, K1, K12, K14, K16, K17, K20, K21 and K22. The global jitter, accelerometer and pressure data were all collected simultaneously with the wavefront measurements at 60 kHz for 10 seconds, a total of 600,000 data points were obtained for each case.

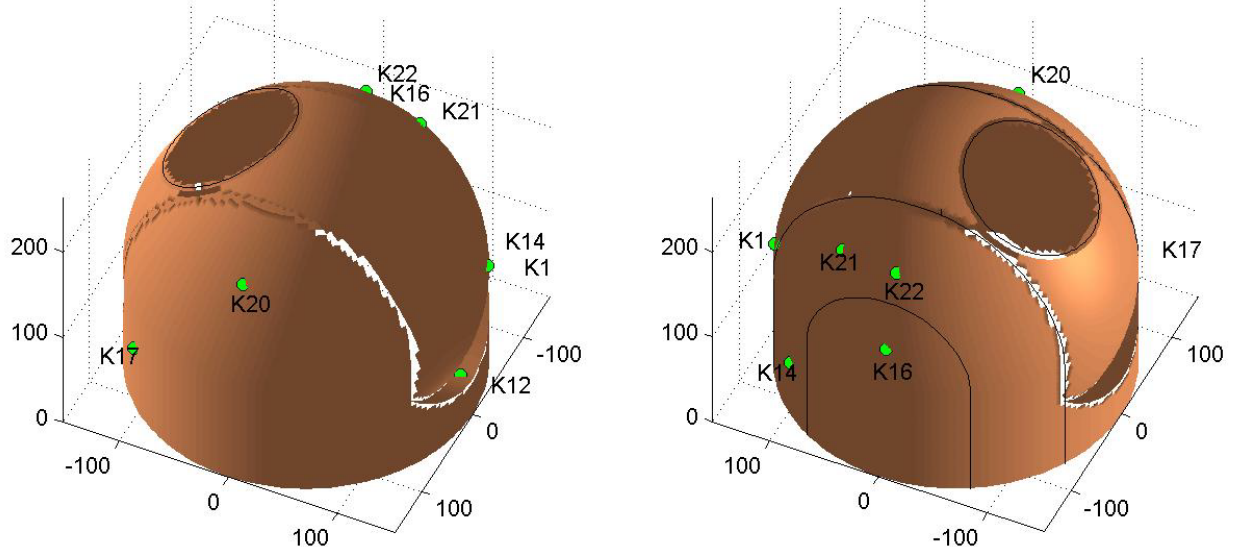


Figure 3: Pressure sensor locations used for this experiment.

### III. Data Reduction

#### *Linear Stochastic Estimation*

The Linear Stochastic Estimation technique was used to extract the aero-optical jitter for the global jitter by estimating and subtracting the mechanically-related jitter. This technique generates an estimate of a measured quantity using a set of other measured quantities. It does this using the correlation between a quantity to be estimated and the additional measured quantities through the cross correlation tensor of the additional quantities. The technique was developed by Adrian [12], and it can be written as

$$\tilde{x}_i = L_{ij} y_j, \quad (1)$$

$$\text{where } L_{ij} = \langle x_i y_k \rangle \langle y_j y_k \rangle^{-1}. \quad (2)$$

Here, a measured signal,  $x_i$ , (mechanically-related jitter) is approximated using a linear sum of other measurements,  $y_i$ , (accelerometers) multiplied by the estimation coefficient matrix,  $L_{ij}$ . The coefficients are determined from the correlations between the signals as given by the  $L_{ij}$ -matrix. For this experiment, LSE technique was applied in the Fourier domain, so the estimation matrix,  $L_{ij}$ , becomes a function of frequency. This method has several significant advantages. It makes no assumption about the relationship between the measured quantities; it only utilizes the statistical correlation between them. The coefficients of the estimation matrix automatically account for any dimensional differences between the measured quantities (to the point of accounting for calibration coefficients automatically). Finally, the estimation matrix only needs to be solved once, making the LSE technique computationally-effective. This technique has been previously used to estimate the aero-mechanical contribution to

beam jitter by correlating jitter measurements and accelerometer measurements [7]. It was also used to estimate the unsteady force applied to the turret using a series of point pressure measurements in [10].

### **Proper Orthogonal Decomposition**

To better understand the instantaneous pressure field,  $p(s,t)$ , where  $s$  is the point of the turret, it is useful to decompose the pressure field into a linear combination of orthogonal pressure modes, using a Proper Orthogonal Decomposition (POD) technique [13], as

$$p(s,t) = \sum_n a_n(t) \varphi_n(s) \quad (1)$$

$$\text{where } a_n(t) = \int_S p(s,t) \varphi_n(s) ds, \quad \overline{a_n(t) a_m(t)} = \lambda_n \delta_{nm} \quad (2)$$

and spatial POD modes,  $\varphi_n(s)$ , and corresponding eigenvalues or mode energies,  $\lambda_n$ , are solutions of an integral equation,

$$\int_S R(s,s') \varphi_n(s') ds' = \lambda_n \varphi_n(s), \quad R(s,s') = \overline{p(s,t) p(s',t)} \quad (3)$$

### **Pressure Field Estimation**

The instantaneous unsteady pressure field in this experiment was estimated using a combination of the LSE and POD techniques. From the PSP experiment described in [8,9,10], the pressure modes on the turret for different window angles were obtained. Using data from that experiment, the LSE technique was used to reconstruct the unsteady pressure field over the turret from present unsteady pressure measurements at few sparse points,  $s_k$ ,

$$\tilde{p}(s,t) = \sum_k L(s,s_k) p(s_k,t), \quad L(s,s_k) = \langle p(s,t) p(s_k,t) \rangle \langle p(s_k,t) p(s_k,t) \rangle^{-1}. \quad (7)$$

Using the POD representation of the pressure field at the sensors' locations,  $p(s_k,t) = \sum_n a_n(t) \varphi_n(s_k)$ ,

Eq.(7) can be rewritten as,

$$\tilde{p}(s,t) = \sum_k L(s,s_k) \sum_n a_n(t) \varphi_n(s_k) = \sum_n a_n(t) \sum_k L(s,s_k) \varphi_n(s_k) = \sum_n a_n(t) \tilde{\varphi}_n(s), \quad (8)$$

where

$$\tilde{\varphi}_n(s) = \sum_k L(s,s_k) \varphi_n(s_k) \quad (9)$$

is a reconstruction of the  $n$ -th POD mode using the sparse array of the sensors.

Figure 4 shows an example of the reconstruction of the POD Modes 1, 2, 3 and 8 for the flat-window case,  $Az = 0$  degrees, with the actual POD modes in the top row and the reconstructed POD modes in the bottom row. The sensor locations are also presented in Figure 4, bottom row, as circles. The first two reconstructed modes are almost identical to their actual counterparts. Reconstructed Mode 3 exhibits many similar features to the actual mode, but is different in some areas, like the left side of the turret near the ‘‘gap’’. Mode 8 is entirely missing two features: the structures near the turret apex and to the left of the downstream ‘‘smile’’. It only resolves activity in the ‘‘smile’’ itself to any appreciable accuracy. The LSE technique correlates the pressure at a specific location on the turret with all other locations. In these poorly-reconstructed regions, there are no nearby pressure sensors and there is not enough statistical correlation with other locations to obtain an accurate reconstruction in these regions.

In order to estimate the error in the pressure reconstruction due to the sparseness of the unsteady pressure sensors on the turret, an absolute error,  $Err(n)$ , was computed between the actual and reconstructed POD modes,

$$Err(n) = \int_S (\varphi_n(s) - \tilde{\varphi}_n(s))^2 ds \quad (10)$$

The errors for the first 10 POD modes at different azimuthal angles are given in Figure 5. The first and the second POD modes for  $Az = 0^\circ$  were correctly reconstructed from the sparse array of the sensors, while the higher modes are not, consistent with the results presented in Figure 4.

To correlate the POD modes with the global beam jitter, the temporal coefficients,  $a_n(t)$ , must be reconstructed from the sparse pressure measurements. From Eq. (4) and Eq. (7) it follows that,

$$a_n(t) = \int_S \tilde{p}(s,t) \varphi_n(s) ds = \int_S \left( \sum_k L(s, s_k) p(s_k, t) \right) \varphi_n(s) ds. \quad (11)$$

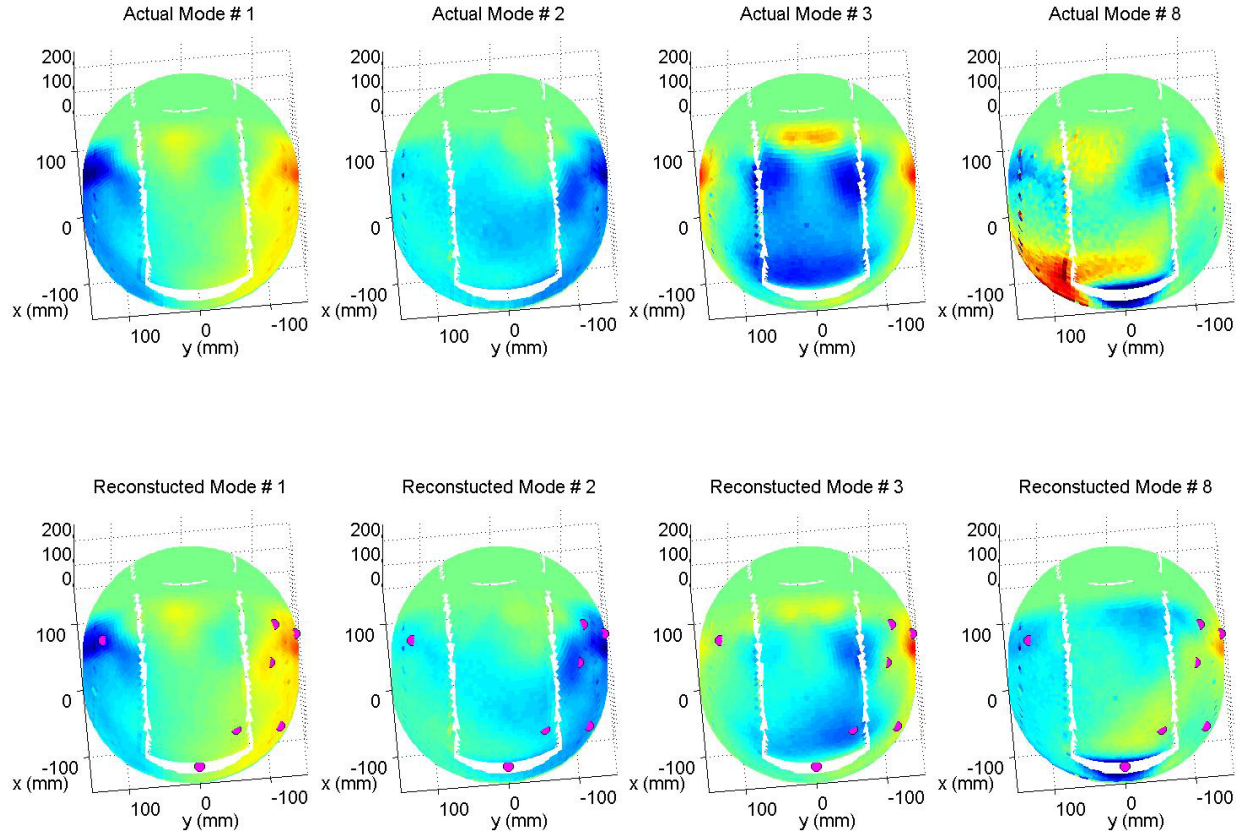


**Figure 4. The POD modes obtained from the PSP test [9], top, and the reconstructed modes using a sparse array of point pressure measurements, bottom, for  $Az = 0^\circ$ . Sensor locations are marked by magenta circles; flow goes along x-axis from positive to negative values.**

Eq. (11) can be re-arranged to

$$a_n(t) = \sum_k p(s_k, t) \left( \int_S L(s, s_k) \varphi_n(s) ds \right) = \sum_k p(s_k, t) c(s_k), \quad (12)$$

where

$$c(s_k) = \int_S L(s, s_k) \varphi_n(s) ds. \quad (13)$$

From the combination of Eq. (9) and Eq. (13), the dominant POD pressure modes and coefficients can be reconstructed using only a sparse array of pressure measurements. For our current experiment, under the assumption

that the flow field isn't different from the flow field in the experiment performed for [8,9,10], the POD modes and coefficients are reconstructed using the correlation matrix  $L$ , Eq (7).

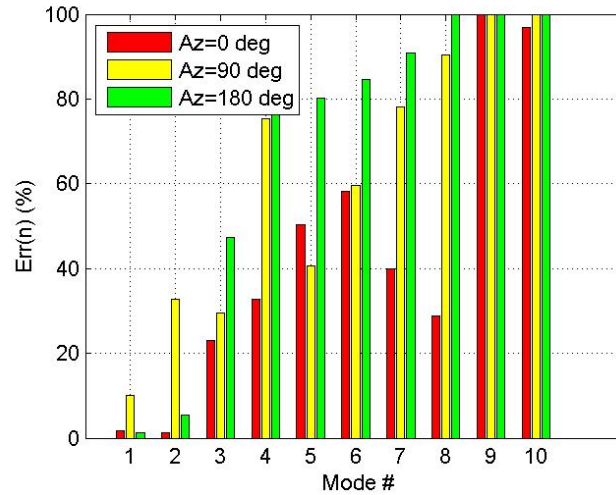


Figure 5. The absolute error in the reconstructed POD modes for  $Az = 0^\circ$ .

#### IV. Results

##### *Pressure Comparison between PSP and Pressure Sensors*

In order for this experiment to be compared with prior work, in particular with the PSP experiment [9], the pressure spectra must be compared at the same locations on the turret. A comparison of the pressure spectra at several given turret locations for both the PSP test and the second tunnel test is shown in Figure 6.

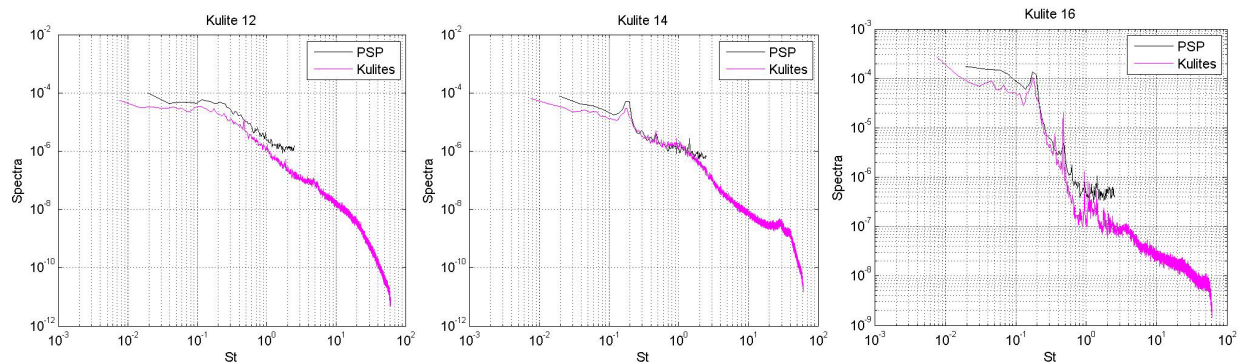


Figure 6: Pressure spectra comparison between PSP test and tunnel test.

The pressure sensor numbers correspond to the pressure sensor locations shown in Figure 3. These unsteady pressure data were collected at  $Az = 0^\circ$ . For each location, the general shape of the spectra is reasonably consistent between the PSP tests and the present tunnel tests. Figure 6, left, shows the pressure sensor K12, which resides in “smile” on the downstream half of the turret. The pressure sensor K14, Figure 6 middle, also is located downstream on the turret, in the separated wake. The spectral shapes of these pressure sensor spectra match the PSP-spectra rather well, with the pressure sensor K12 having a slight amplitude difference. At this azimuth angle, the pressure sensor K16, Figure 6 right, is aligned with the side of the turret near the unsteady separation line [9]; this separation line has a corresponding spectral peak at  $St = 0.15$ , also observed in [9,10].

##### *Surface Pressure and Flow Features*

Before studying the relation between the unsteady pressure on the turret and the aero-optical jitter, it is useful to describe the unsteady pressure environment on the turret and to see how it is modified for different locations of the flat-window and “smiles”, relative to the flow. Figure 7 shows the pressure spectra for various sensor locations at

the window azimuthal angle of  $180^\circ$ , selected to highlight different regions of the flow around the turret. As was previously shown using the PSP experiment [9], the unsteady movement of the separation line is characterized by a broad peak at  $St = 0.15$ . At this Strouhal Number, there is a distinct broad peak for all of the pressure sensors except the green sensor. The largest fluctuations at  $St = 0.15$  occur at the blue and black pressure sensors, both of which lie directly in the region near the separation line. Pressure fluctuations in the separated wake are shown by the magenta pressure sensor in Figure 7. Comparing the red sensor, which is located on the upstream portion of the turret, and magenta sensor, located on the downstream portion of the turret, there is an overall increase in pressure fluctuations from  $St = 0.15$  to  $St = 5$  for the magenta sensor. Specifically, there is a broad peak with a peak near  $St = 1$ . These pressure fluctuations are from vortical structures formed on both sides near the base of the turret [9], see Figure 1. The smallest pressure fluctuations measured at this angle occur in the front “smile”, Figure 7, the green sensor. At this location on the upstream half of the turret, the flow is attached and the low pressure levels indicate that there isn’t significant turbulent activity occurring locally in the front “smile”. Therefore, pressure fluctuations at this point are mostly the result of the global Biot-Savart induction from the global unsteady field. It has been hypothesized in this paper that the global pressure fluctuations on the upstream portion of the turret are predominantly resulted from the unsteady separation line on the turret, the separated wake “breathing”, the vortical structures near the downstream portion of the turret base and pressure fluctuations induced by the necklace vortex. The indirect influence of these effects on the unsteady pressure on the upstream portion of the turret can be in the pressure spectra for the red and cyan pressure sensors in Figure 7. The influence from the unsteady separation motion is indicated by the peak around  $St = 0.15$ , while the vortical structures on the downstream portion of the turret are responsible for the smaller second broad peak near  $St = 1.0$ .

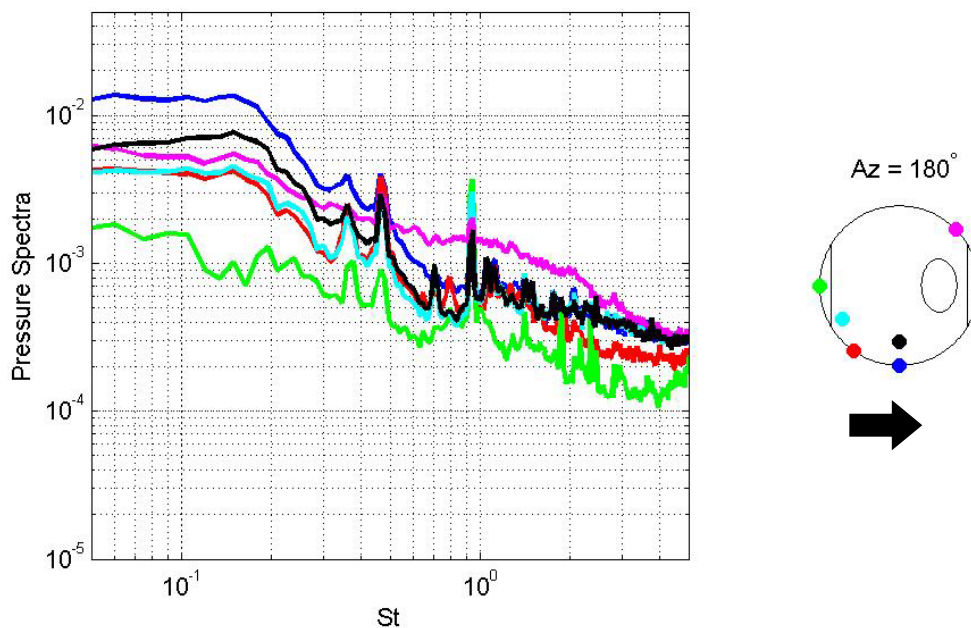


**Figure 7: Pressure spectra at various locations on the turret for  $Az = 180^\circ$ . The arrow indicates the flow direction.**

In the PSP experiment [9], it was shown that the orientation of the “smiles” on the turret, relative to the flow, had a substantial impact on the pressure fluctuations around the turret. Representative examples of the unsteady pressure fields for  $Az = 90^\circ$  degrees, obtained using a fast-response PSP [9], are shown in Figure 8. At this side-looking window angle, geometric discontinuities due to the “smiles” create additional traveling vortical structures downstream of the “smiles”. Local pressure spectra at similar flow-related locations on the turret for  $Az = 90^\circ$  and  $Az = 180^\circ$  are shown in Figure 9. The PSP experiment [9] showed an increase in the magnitude of the pressure fluctuations associated with the separation line on the turret when the “smiles” were oriented in the cross-stream direction, which corresponds to the window azimuthal angle of  $90^\circ$ . This effect can also be observed in the present experiment by comparing pressure spectra in Figure 9 for the blue and the red sensor locations ( $Az = 180^\circ$ ) with the cyan ( $Az = 90^\circ$ ) sensor locations. The peak at  $St = 0.15$  is of a larger magnitude at an azimuthal angle of  $90^\circ$ . Additionally, there is a large increase in fluctuations in the high-frequency range between  $St = 0.3$  and 2. In [9]

it was shown that the edges of the “smiles” provide a geometric discontinuity near the separation line, which was not present when “smiles” were located in the front of the turret for  $Az = 180$  degrees. Due to this geometric discontinuity, a shear layer forms over the “smile” at  $Az = 90^\circ$  and is responsible for the broadband increase in pressure fluctuations for the cyan pressure location. The “smiles” also alter flow downstream at  $Az = 90^\circ$ . To see this, let’s consider the magenta and the green sensor locations, which are at similar, relative to the flow, locations on the turret. With the “smiles” aligned streamwise ( $Az = 180^\circ$ ), Figure 9, the green sensor, there is a broad, but weak, peak from  $St = 0.3$  to  $St = 2$ . With the “smiles” aligned cross-stream ( $Az = 90^\circ$ ), the magenta sensor, there is also a broad peak at this frequency range, but the magnitude of the pressure fluctuations is significantly increased. Also, the peak location for this broad peak is shifted toward a smaller value of  $St = 0.7-0.8$ . So, the sharp edge of the “smiles” adds additional vortical structures into the flow near the base of the turret for the  $Az = 90^\circ$  case.

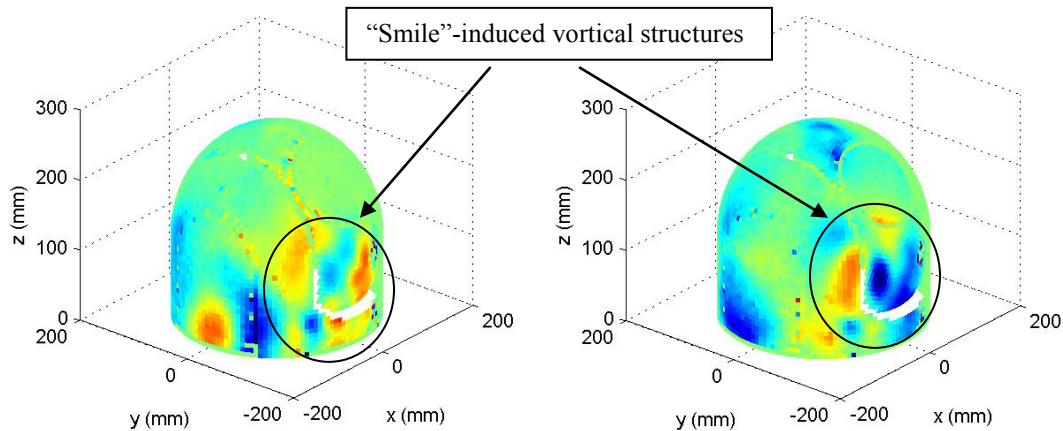


**Figure 8. Representative instantaneous pressure fields for  $Az = 90$  degrees, measured using fast-response pressure-sensitive paint [9]. The flow goes along x-axis from positive to negative values.**

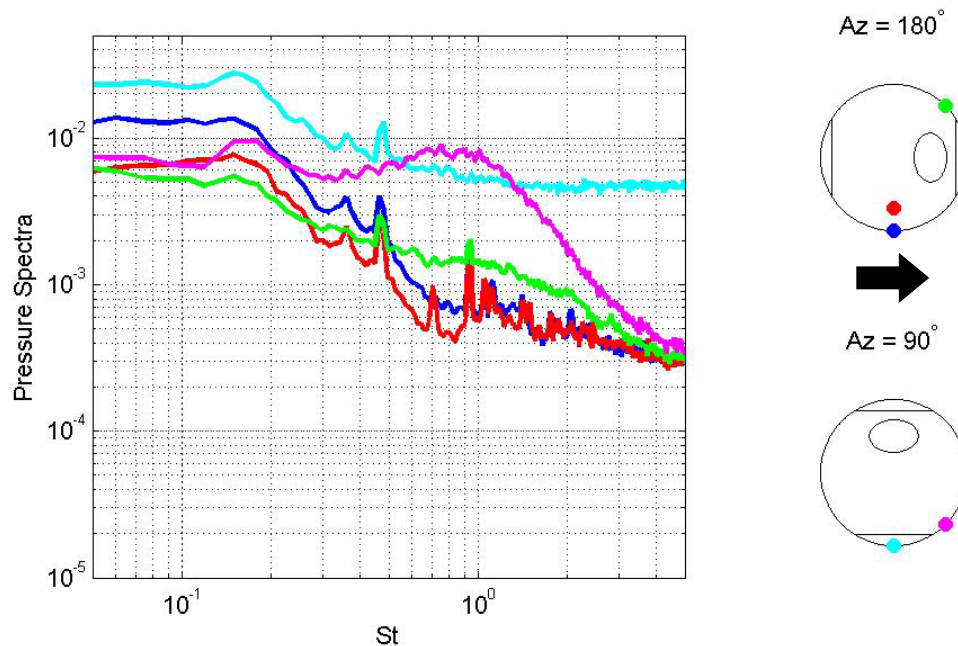


**Figure 9: A comparison of local pressure spectra for  $Az = 90^\circ$  and  $Az = 180^\circ$  to show the effect of the “smiles”. The arrow indicates flow direction.**

The location of the flat window, relative to the flow, also impacts the flow features around the turret. Figure 10 shows local pressure spectra at locations near the downstream portion of the base of the turret for  $Az = 0^\circ$  and  $Az = 180^\circ$ . For the red and the blue locations, the flat window is located upstream, and it is located downstream for the green location. The red and the blue spectra both have a larger magnitude broad peak between  $St = 0.5$  and  $St = 2$ ,

compared to the green spectrum. As it was discussed before, this broad peak is associated with the vortical structures near the turret base. The PSP experiment [9] showed additional turbulent structures convecting off the top of the turret with the flat window oriented in the upstream direction, see representative pressure fields in Figure 11; the slope discontinuity of the flat window causes a premature separation to occur on top of the turret. It is likely that the premature separation modifies the separation region downstream of the turret, which results in intensifying the vortical structures at the downstream portion of the turret base.

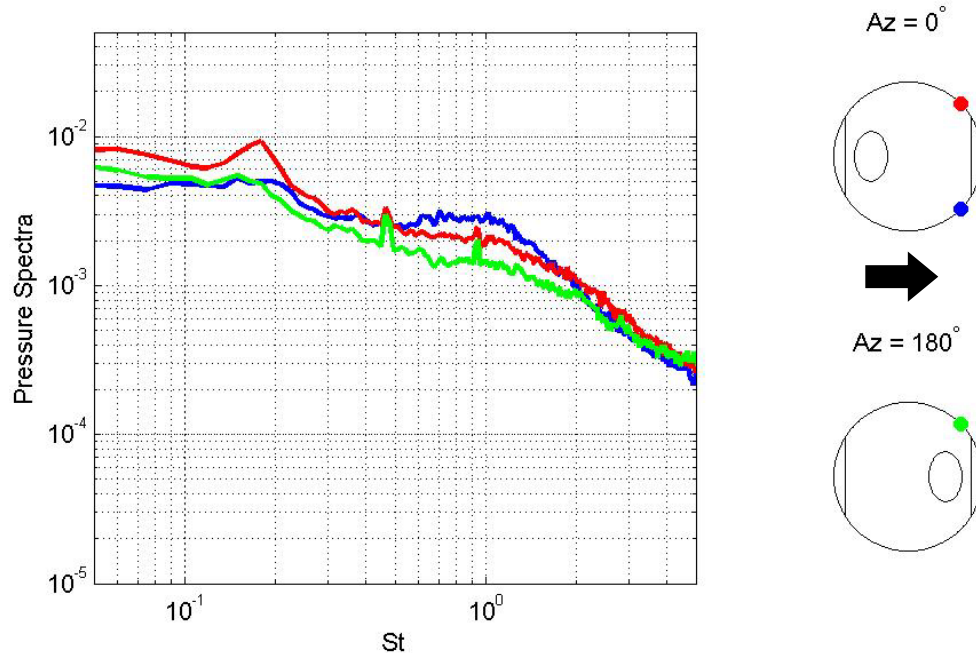


**Figure 10: Local pressure spectra at  $Az = 0^\circ$  and  $Az = 180^\circ$  showing the effect of flat window location. The arrow indicates flow direction.**

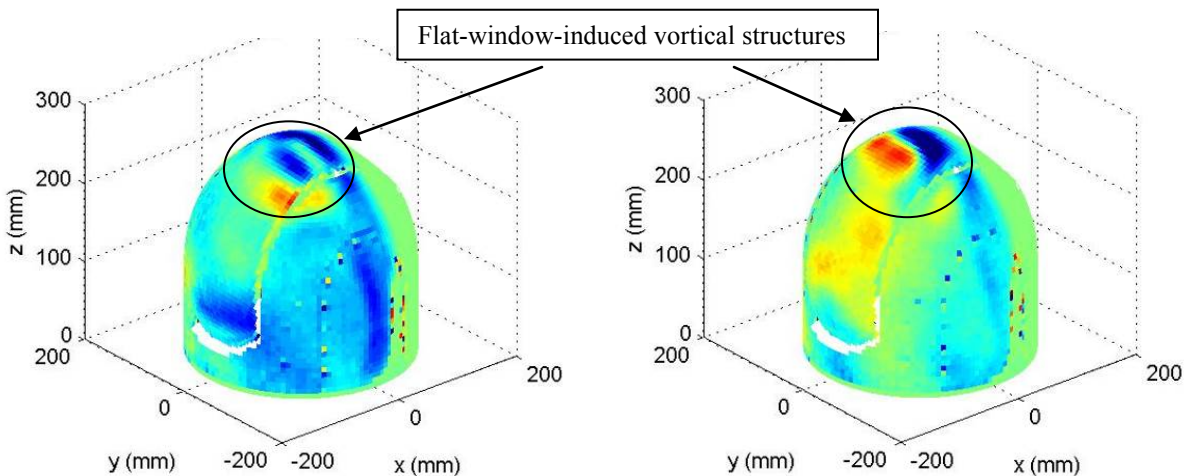


**Figure 11. Representative instantaneous pressure fields for  $Az = 0$  degrees, from [9]. The flow goes along x-axis from positive to negative values.**

### Total Jitter Analysis

The total jitter, aero-optical jitter and mechanical jitter are shown for both  $Az = 0^\circ$  and  $Az = 90^\circ$  in Figure 12. These plots show the Y-direction jitter, which corresponds to the vertical component in the aperture frame of reference. The mechanical jitter component was estimated using the LSE-based technique, Eq. (1), and it was subtracted from the global jitter to obtain the aero-optical jitter. The mechanical jitter has several dominant regions

for both cases. At  $Az = 0^\circ$ , the aero-optical jitter dominates except for a region between  $St = 0.3$  and  $St = 2$ . At  $Az = 90^\circ$ , the mechanical jitter dominates not only in the same range, but also at the high frequency range of  $St < 2$ . For  $Az = 90^\circ$ , the aperture is oriented in the cross stream direction. The most energetic pressure mode, shown in Figure 4 far left, is asymmetric in the cross-stream direction, which means the mode will cause unsteady forcing in the cross stream direction, as shown in [10]. This forcing likely induces the turret into “rocking” motion in the cross stream direction, driving the increase in y-component mechanical jitter.

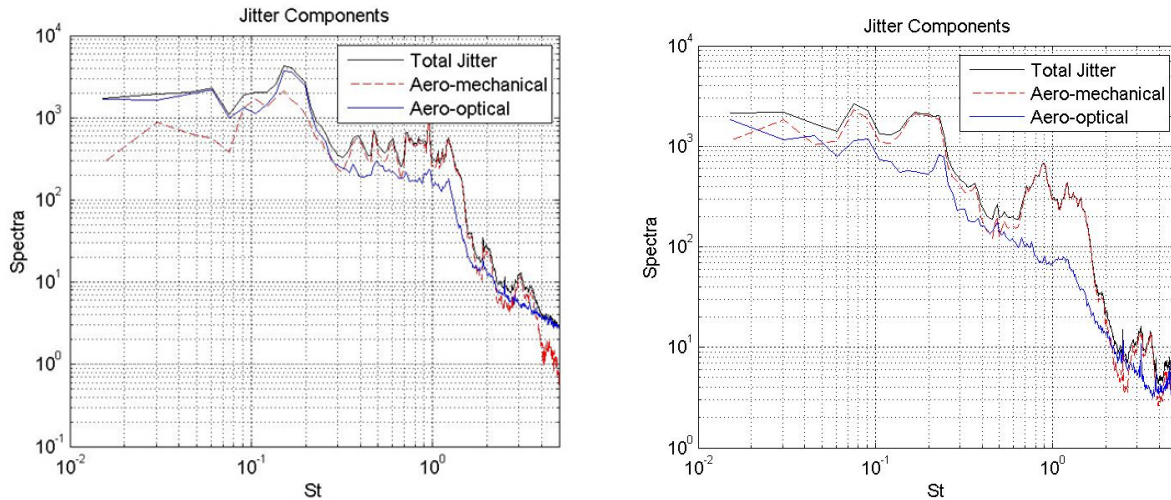


Figure 12: Spectra of different jitter components in Y-direction for  $Az = 0$ , left, and  $Az = 90$ , right.

The total amount of the aero-optical and the mechanical jitter, normalized by  $\rho M^2$ , is given in Figure 13. Consistent with the spectra in Figure 12, both X- and Y-components of the mechanical jitter are significantly larger for  $Az = 90^\circ$  than for  $Az = 0^\circ$  or  $180^\circ$ ; both  $Az = 0^\circ$  and  $Az = 180^\circ$  have very similar amounts of the mechanical jitter. This is to be expected as the turret geometry, specifically the orientation of the “smiles” with respect to the flow direction, is the same both cases. The only geometrical difference, which is introduced by the flat aperture facing upstream or downstream, has almost no impact on the levels of the induced mechanical jitter. For the aero-optical jitter component,  $Az = 0^\circ$  case has the largest total RMS contribution from aero-optical effects, with  $Az = 180^\circ$  case experiencing the least.

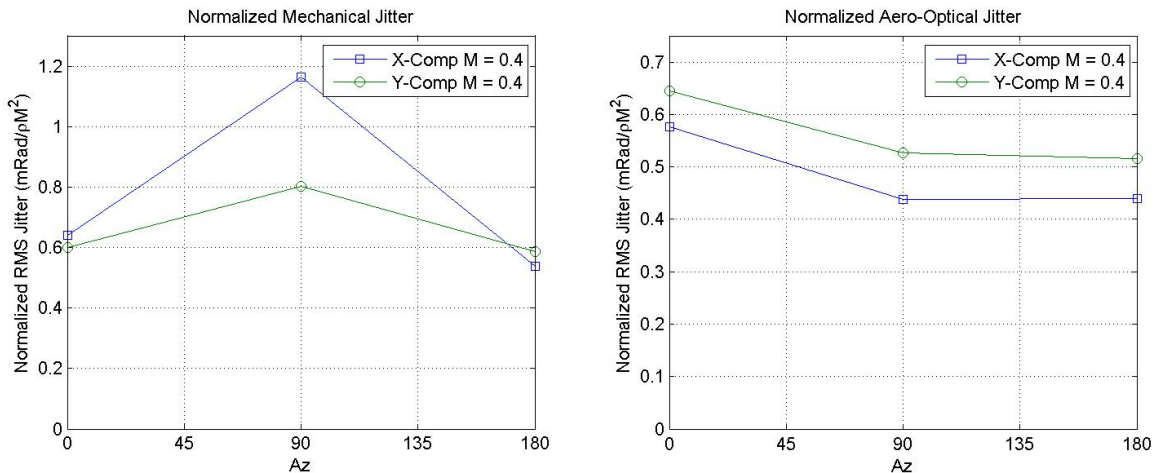


Figure 13: Normalized RMS of the mechanical and the aero-optical jitter as a function of viewing angle.

The aero-optical jitter is driven by the turbulent flow field, so these global aero-optical distortions are the result of the laser beam propagating through the density field that has a net linear time-dependent density gradient across the aperture. Sources for this density gradient include local changes in pressure/density related to the turbulent structures directly over the aperture, as well as global Biot-Savart induced pressure/density variations. For instance,

for  $Az = 0^\circ$ , the laser beam propagates through the attached flow and the dominant source of aero-optical jitter is the unsteady pressure variations from the global pressure field around the turret due to Biot-Savart induction. At  $Az = 180^\circ$ , the beam looks through the separated wake, so the vortical structures in the separated flow field has the dominant effect on the aero-optical jitter.

### *Aero-optical Jitter Analysis*

#### $Az = 0^\circ$

A comparison of aero-optical jitter results from this experiment and from another experiment [14] is shown in Figure 14. The turret geometry between the two experiments was the same, but the turret in [14] did not have the “smiles”. At  $St < 0.3$ , the shape of the spectra between both experiments is similar, although with an amplitude mismatch. For the X-component of the aero-optical jitter, a double peak occurs at or below  $St = 0.2$ , while a single peak occurs in the Y-component. At  $St > 3$ , there is also similarity between the two experiments. The primary difference occurs between  $St = 0.3$  and  $St = 2$ . For the current experiment, the spectral energy remains almost constant until  $St = 1.5$ , at which point there is a sharp fall-off in the spectra. For the spectra from [14], the fall-off occurs at a lower frequency of  $St = 0.2$ . It is thought that the “smiles” are the primary reason for this difference.

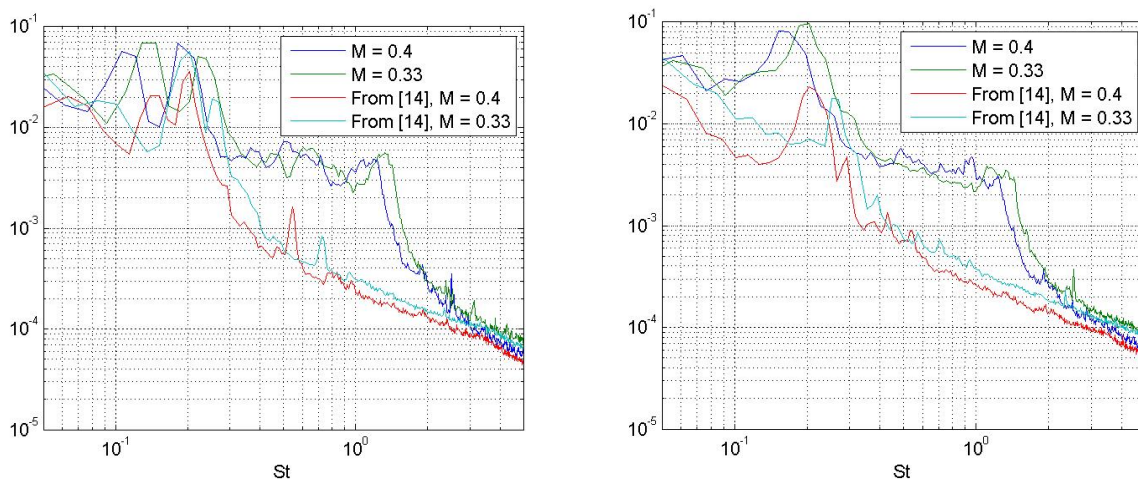


**Figure 14: Comparison of the aero-optical jitter spectra for this experiment and from [14]. X-component is left, Y-component is right. Azimuth angle is  $0^\circ$ .**

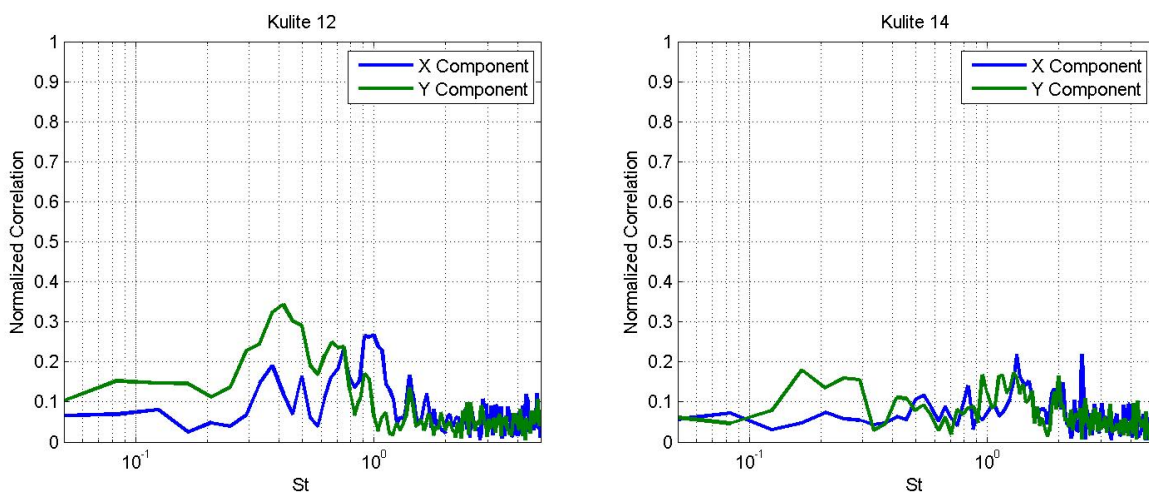


**Figure 15: Correlation between the aero-optical jitter and the unsteady pressure from pressure sensor K12, located in the wake, at the “smile” and K14, in the wake near the turret base for  $Az = 0^\circ$ .**

At this window viewing angle, there is no significant aero-optical structures located at or passing directly over the flat window, so the global aero-optical jitter should be dominated by the indirect Biot-Savart induction from the necklace vortex and the separated wake. To investigate this link, local pressure measurements at two sensor locations, K12 and K14 were correlated with the aero-optical jitter at  $Az = 0^\circ$ , shown in Figure 15. At this azimuthal angle, K12 is located inside the downstream “smile” on the turret inside the separated wake, where the recirculating flow impinges on the turret. There is a broad correlation peak between  $St = 0.3$  and  $St = 1$  with the y-component of the aero-optical jitter, see Figure 15, left. Given the location of K12, it is likely that this vertical y-component of the aero-optical jitter in this frequency range is driven by the vertical displacement or “breathing” of the separated wake, as the wake expands and contracts in vertical direction, which causes the global flow displacement and, consequently, variations in the global pressure field. These pressure fluctuations induce density changes which then appear as the aero-optical jitter. For the x-component of the aero-optical jitter, the same pressure sensor shows a somewhat weaker correlation at a higher frequency near  $St = 1$ . As shown in Figure 7, this frequency range might be connected to the vortical structures on both sides of the downstream portion of the turret. However, from Figure 15, right, there is no significant correlation between K14, located near these vortical structures, with either of the jitter components at  $St = 1$ . Because there is only a weak correlation with pressure sensor K14 at this frequency range, it’s more likely that the jitter is related to a different mechanism. One possible explanation would be the global motion of the turret separated wake in the cross stream direction, which is not directly detected by the present arrangement of the pressure sensors on the turret surface.

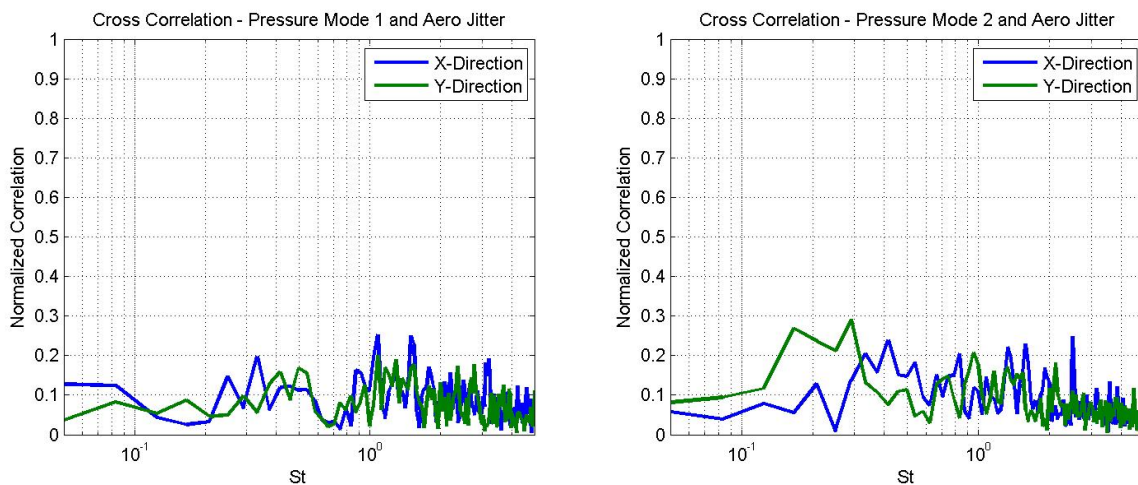


**Figure 16: Correlation between the aero-optical jitter and the first two reconstructed pressure POD modes.  $Az = 0$  degrees.**

Another way to study the possible correlation between the jitter and the separated wake dynamics is to correlate the aero-optical jitter to the first two dominant POD modes, which describe the unsteady behavior of the separation line on the turret and are related to the global motion of the separated wake [9]. Mode 1, shown in Figure 4, top far left, is anti-symmetric in the cross-stream direction; the anti-symmetry indicates that the motion of the separation line on either side of the turret is out-of-phase with the opposite side, which might be related to the horizontal motion of the separated wake. Mode 2, shown in Figure 4 top middle left, is almost symmetric in the cross-stream direction and is likely to be related to the vertical motion of the separated wake. The correlation between the first two pressure POD modes and the aero-optical jitter is shown in Figure 16. The X-direction of the aero-optical jitter should be affected by bulk changes of the wake in the cross-stream direction at this azimuthal angle. As there is no significant correlation between POD mode 1 and the x-component of the jitter, it suggests that this bulk wake motion is likely not directly related to the motion of the separation line on the turret. As Mode 2 is predominantly spanwise-symmetric, it should not significantly influence the x-component of the jitter either, as can be seen in Figure 16, right.

Similarly, the anti-spanwise-symmetric Mode 1 does not affect the y-component of the jitter, see Figure 16, left. However, the y-component of the aero-optical jitter correlates with Mode 2 in the range of frequencies between  $St = 0.15$  and  $St = 0.3$ . This frequency range, while somewhat close, is still different from the frequency range of the correlation between the jitter and the sensor K12, located on the bottom of the turret base, see Figure 15, left. This observation suggests that the separated wake has a complex dynamics and different parts of the wake influence the

pressure field over the upstream portion of the turret at different frequency ranges, centered around  $St = 0.2, 0.4$  and  $1.0$ .

$Az = 90^\circ$

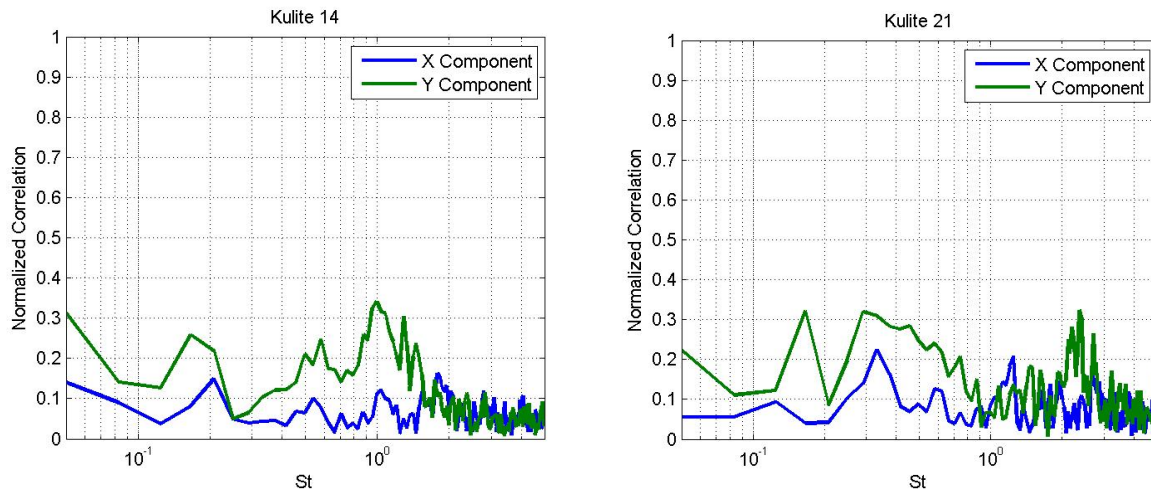


**Figure 17: Left: Correlation between the aero-optical jitter and the unsteady pressure from pressure sensor K14, located downstream of the “smile” for  $Az = 90^\circ$ . Right: Correlation between the aero-optical jitter and the unsteady pressure from pressure sensor K21, located in the wake for  $Az = 90^\circ$ .**

At this viewing angle, the forward edge of the flat window trips the flow and the separated bubble forms over the portion of the window [2]. Thus, the jitter at this angle is influenced both directly by turbulent structures over the flat window and indirectly by the unsteady separation line and the separated wake via Biot-Savart induction. The aero-optical jitter at the window location of  $Az = 90^\circ$  was correlated with two pressure sensors, K14 and K21, and the normalized correlation is shown in Figure 17. At this window angle, K14 is located near the vortical structures at the downstream portion of the base of the turret. As it shown in Figure 17, left, the unsteady pressure at this sensor location has very little correlation with the x-component of the aero-optical jitter, suggesting that at this window angle, the vortical structures near the base of the turret don’t significantly impact the x-component of the aero-optical jitter. However, there are two frequency regions of a relatively-high correlation with the y-component of aero-optical jitter. The first region at  $St = 0.15$  indicates that there is correlation between the y-component of the aero-optical jitter and the motion of the separation line on the turret. A second peak in correlation between K14 and the Y-component of the aero-optical jitter occurs at higher frequencies between  $St = 0.5$  and  $St = 1.5$ . This is the same frequency range associated with the vortical structures formed downstream of the “smile” at the base of the turret. From Figure 9, it was shown that pressure fluctuations in this range are substantially increased for the window angle of  $Az = 90^\circ$  compared to the window angle of  $Az = 0^\circ$  or  $Az = 180^\circ$ . As these structures are located near the base of the turret and do not convect directly over the aperture, it is likely the vortex induction effect which influences the vertical aero-optical jitter.

A correlation between the aero-optical jitter components and K21, located in the separated wake just downstream of the separation line, is shown in Figure 17, right. As with K14, there is correlation between the local pressure and the y-component of aero-optical jitter at  $St = 0.15$ , associated with the separation line motion on the turret. There is additional correlation in the y-component between  $St = 0.2$  and  $St = 0.9$ . Similar frequency ranges were observed in the correlation between the y-component of the jitter and K12, located near the separation line on the opposite to the window side, see Figure 18. The second frequency range is similar to the range observed in Figure 15, left, also suggesting that the vertical wake motion might be responsible for the y-jitter at this window angle. The x-component of the aero-optical jitter shows a small overall correlation with both K21 and K12 sensors.

For this viewing angle, POD modes were reconstructed with a fairly large error for the present sensor arrangement, as was shown in Figure 5, so the correlations between the jitter and reconstructed dominant POD modes might be contaminated by the improperly-reconstructed POD modes and therefore are not presented here.

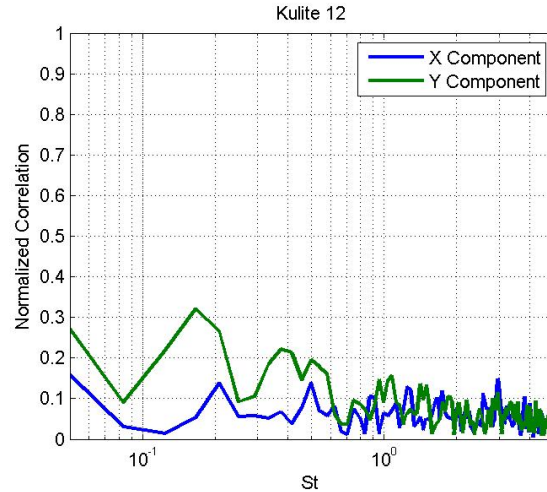


**Figure 18: Normalized Correlation between the aero-optical jitter and the unsteady pressure from pressure sensor K12, located in a “smile” for  $Az = 90^\circ$ .**

### $Az = 180^\circ$

At this angle, vortical structures are formed downstream of the separation line and convect directly over the laser beam. Thus, the aero-optical jitter at this angle is dominated directly by these local vortical structures and less affected by the global wake motion. The correlation between K21 and the aero-optical jitter for the window azimuthal angle of  $Az = 180^\circ$  is shown in Figure 19, left. At this angle, the sensor is located slightly upstream of the separation line on the side of the turret. The sensor is relatively distant from the optical window and any correlation is likely the result of global pressure changes, primarily due to the wake motion, as opposed to local effects. There is a weak correlation for both the x- and y-components of the aero-optical jitter between  $St = 0.2$  and  $0.5$ ; this frequency range was associated to the vertical wake motion for other window angles, see Figure 15, left and Figure 17, right. When correlating the jitter with the nearby sensor K22, located at the separation line, the weak correlation also shows the weak peak in the similar frequency range for the y-component of the aero-optical jitter, as shown in Figure 19, right.

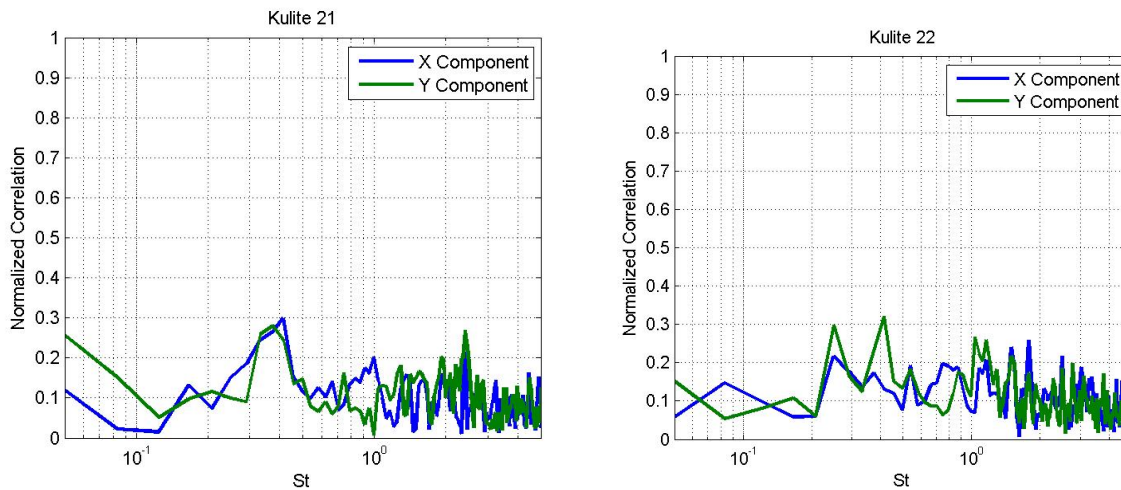


**Figure 19: Left: Correlation between aero-optical jitter and unsteady pressure from pressure sensor K21, located upstream on the side of the turret for  $Az = 180^\circ$ . Right: Correlation between aero-optical jitter and unsteady pressure from pressure sensor K22, located on the side of the turret for  $Az = 180^\circ$ .**

The first three actual and the reconstructed POD modes for this azimuthal angle are shown in Figure 21. The first two modes were reconstructed properly, as the reconstruction error is fairly small, see Figure 5. As for the case of the azimuthal angle of 0 degrees, the first POD mode represents the anti-spanwise-symmetric mode and it is likely to be linked to the horizontal motion of the separated wake. The second POD mode is spanwise-symmetric and is

related to the vertical displacement of the separated wake. The correlations between the first two POD mode and different component of the aero-optical jitter at  $Az = 180$  degrees are presented in Figure 20. There is no significant correlation between global POD modes and the jitter, except at the frequencies between  $St = 0.2$  and  $0.5$ , where the x-component of the aero-optical jitter is weakly correlated with the first POD mode and the y-component of the jitter is correlated with the second POD mode. These results are consistent with the correlations between the individual pressure sensors K21 and K22 with the jitter, shown in Figure 19, which also suggested a weak correlation between the jitter and the wake motion.

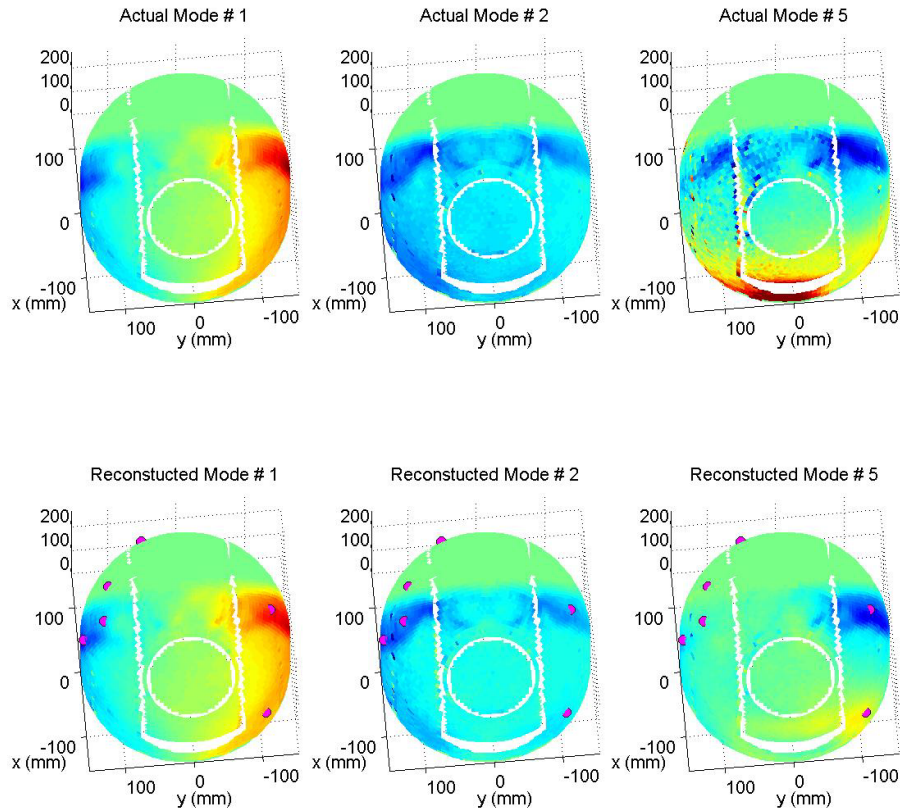


**Figure 21.** The POD modes obtained from the PSP test [9], top, and the first three reconstructed modes using a sparse array of point pressure measurements, bottom, for  $Az = 180^\circ$ . Sensor locations are marked by magenta circles, flow goes along x-axis from positive to negative values.

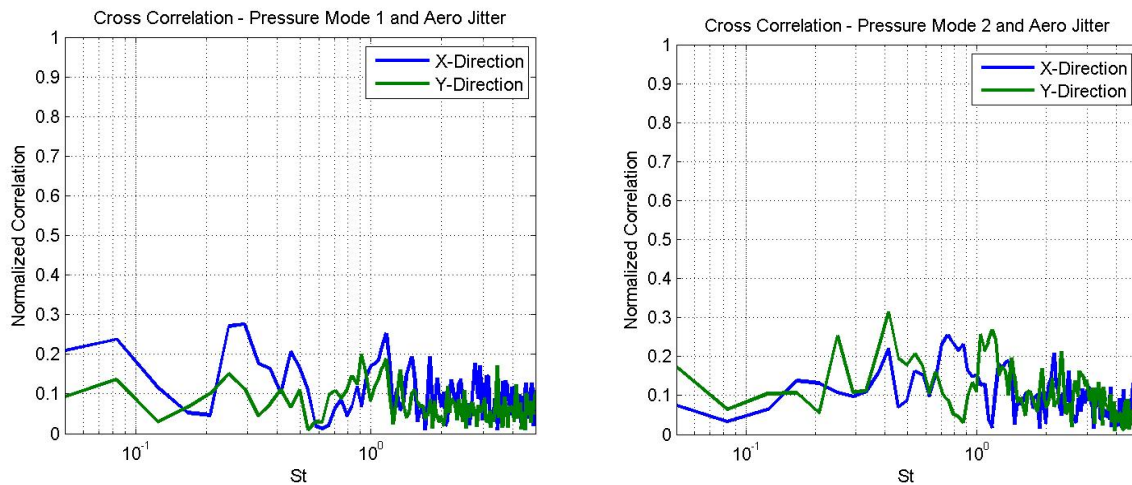


**Figure 20:** Correlation between the aero-optical jitter and the first two reconstructed pressure POD modes.  $Az = 180$  degrees.

K17 is located in the wake near the base of the turret and there is no significant correlation with either the x- or y-components of aero-optical jitter with K17, see Figure 19, right. As this pressure sensor is near the vortical structures formed at the base of the turret, it is plausible to conclude that these structures do not significantly impact the aero-optical jitter at this angle.

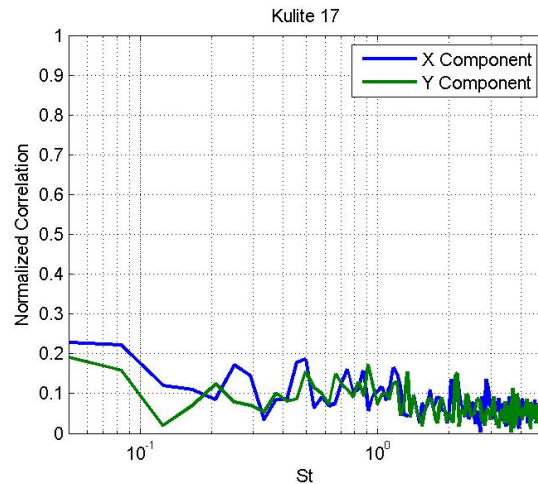


**Figure 22: Correlation between aero-optical jitter and unsteady pressure from pressure sensor K17, located in the wake for  $Az = 180^\circ$ .**

The pressure sensors have shown some correlation with the aero-optical jitter that can be associated with global pressure fluctuations inside the separated wake. To investigate whether local turbulent structures over the aperture drive aero-optical jitter, correlations between higher order, jitter-removed, wavefront modes are performed. The wavefront modes are shown in Figure 23, and the correlations are given in Figure 24. The strongest correlations are with modes 2 and 4. These two modes are characteristic of shear structures convecting over the window. Modes 1 and 3 are related to unsteady defocus and are most likely driven by global effects, like the wake breathing. The correlations for both modes 2 and 4 exhibit a broad peak at  $St = 0.15$  with another broad peak near  $St = 0.4$ . These frequencies were associated with the separation line on the turret and the vertical wake motion, respectively. Based on these observations, there is likely that the y-component of the aero-optical jitter is introduced by the shear structures that formed downstream the separation line at the top of the turret. These vortical-structure are compact and move away from the turret, so do not create significant pressure fluctuations on the turret surface; it explains why there is no significant correlations between the aero-optical jitter and the surface pressure sensors. For instance, from Figure 22, there was a weak correlation at  $St = 0.25$  from K22, which is close to the separation line, and there is a stronger correlation between the jitter and wavefront modes 2 and 4 at the same Strouhal Number, see Figure 24. As K22 lies on the side of the turret and not directly upstream of the aperture, it's possible that it does not fully sense the formation of the vortical structures that drive this aero-optical jitter. Aero-optical aberrations are an integrated phenomenon; they are affected by flow features which can be relatively distant from the turret. This shows that not all aero-optical jitter driving phenomena can be fully investigated or approximated using only measurements on the turret surface.

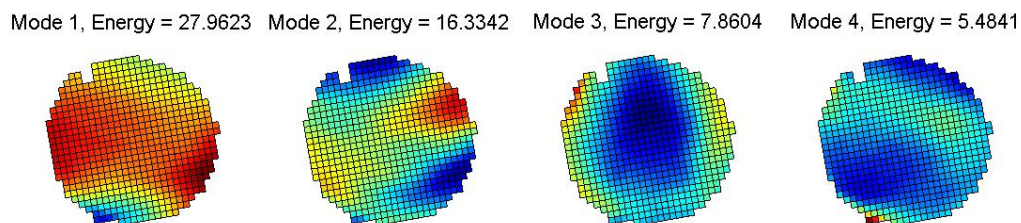


**Figure 23: The first 4 wavefront modes for  $Az = 180^\circ$ , used to investigate local sources of aero-optical jitter.**

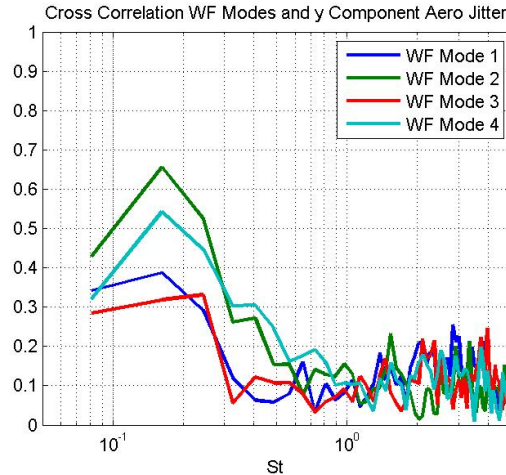


**Figure 24: The correlation between the first 4 wavefront modes and the Y-component of the aero-optical jitter for Az = 180°.**

**Potential Mitigation of Total Jitter**

The correlations between aero-optical jitter and various local pressure sensors were discussed in the previous section. This correlation indicates that the LSE-based technique to isolate mechanical jitter can be also used to reduce the overall jitter levels. By including the local pressure measurements from the sparse array of sensors to the LSE estimate of the jitter, any aero-optical effects correlated with the pressure measurements can be removed as well. This can allow for the development of an open loop FSM-based control system to reduce both aero-optical and aero-mechanical jitter for an airborne laser platform. The result of this combined technique is shown in Figure 25. The addition of pressure sensors to the jitter removal LSE-technique has a similar effect for each investigated angle, further reducing the residual jitter. The additional amount of the jitter removed by including surface pressure data is independent of the angle. Additionally, the magnitude of aero-optical jitter reduction compared to mechanical jitter reduction is small. With a sparse set of pressure sensors at sub-optimal locations, it is possible that one or both of these trends are a result of sub-optimal sampling of the pressure field. With optimized sensor locations for a given viewing angle, a better improvement on the jitter reduction is likely possible. To provide an example of reduction amounts with the current sensor locations, the overall X-component jitter at Az = 90° was reduced from 1.33 mRad/ρM<sup>2</sup> to 0.50 mRad/ρM<sup>2</sup> using accelerometers only and was further reduced to 0.46 mRad/ρM<sup>2</sup> when the sparse pressure sensors were included. This is a substantial improvement even at the relatively small jitter values of a controlled lab setting using a non-location optimized array of pressure sensors.

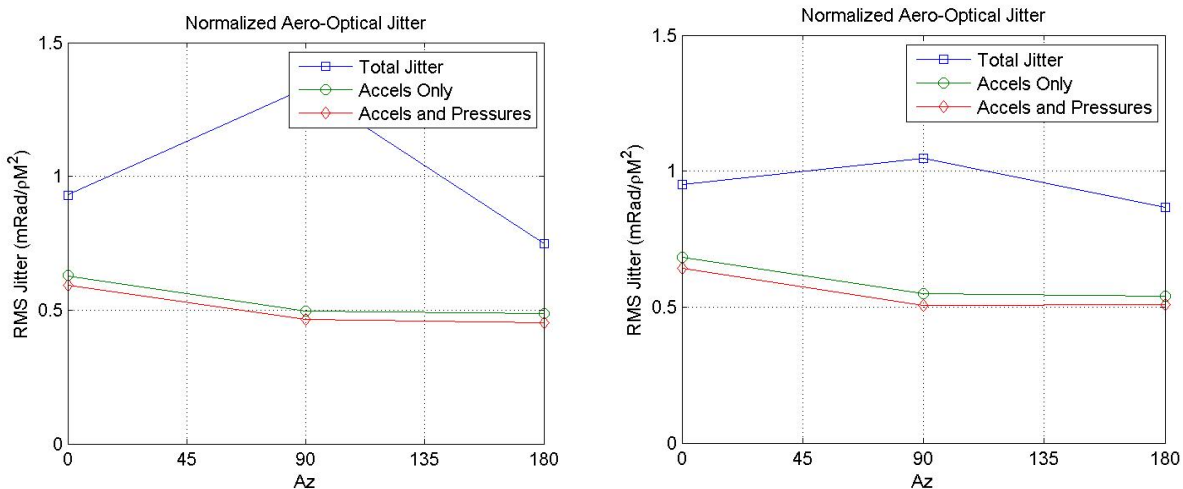


**Figure 25: The total jitter corrected with just accelerometer data and the combination of accelerometer and pressure data for the X-direction, left and Y-direction, right.**

## V. Conclusions

Simultaneous wavefront, jitter and sparse surface pressure measurements were performed on a replica of AAOL turret at the University of Notre Dame. The data were collected for three different azimuthal angles,  $0^\circ$ ,  $90^\circ$  and  $180^\circ$ . The jitter was decomposed into aero-optical and mechanical jitter components using an LSE-based technique. The pressure spectra were compared with a PSP experiment [8, 9, 10] and compared for different azimuthal angles to determine the effects of the turret “smiles” and window location on various flow features around the turret.

The measured aero-optical jitter was directly compared with data from a turret of similar geometry used in the same wind tunnel. The difference between the turrets was the existence of two “smiles” on the AAOL turret. The jitter spectra were similar below  $St = 0.2$  and above  $St = 2$ . Between these ranges, the levels of the aero-optical jitter for AAOL turret with “smiles” were higher than for the turret without the “smile”. It was hypothesized that the “smiles” change flow features and induce additional aero-optical jitter.

Local correlations between the aero-optical jitter and the pressure sensors, as well as correlations with dominant global pressure modes, were performed. The aero-optical jitter was shown to correlate with different flow features depending on the viewing angle. At the window forward-looking angle of  $Az = 0^\circ$ , the vertical aero-optical jitter was dominated by vertical wake breathing effects in the frequency range between  $St = 0.3..0.5$ . For the window side-looking angle of  $Az = 90^\circ$ , y-direction jitter was driven by the moving separation line at  $St = 0.15$  and by vortical structures formed by “smile” discontinuities in the frequency range near  $St = 1$ . For the back-looking angle of  $Az = 180^\circ$ , there was some correlation with the vertical wake breathing in the frequency range  $St = 0.2..0.5$ , but less so than was observed at  $Az = 0^\circ$ . Unlike for the forward- and side-looking window, where the jitter was mostly the result of the temporal changes of the global pressure field via Biot-Savart induction mechanism, with the window looking back through the wake, the aero-optical jitter was primarily driven by compact vortical structures convecting over the window. For  $Az = 0^\circ$  and  $180^\circ$  the x-component of the aero-optical jitter was found to be weakly correlated with the horizontal motion of the wake and, in lesser degree, with the vortical structures on the downstream portion of the turret base in the frequency range near  $St = 1$ .

Utilizing the correlations between the aero-optical jitter and local pressure measurements, the LSE-technique was expanded to include surface pressure measurements to better estimate the total beam jitter. Although the accelerometers alone provided a significant reduction (67%) in the beam jitter, the set of sparse pressure sensors with non-optimal locations provided a further reduction of 11.5%. Using an optimized set of locations for the pressure sensors, a better improvement is expected.

Future work will include using the same technique with additional pressure sensors and/or optimized sensor locations to extract more information about the global pressure field and the driving mechanisms behind aero-optical and mechanical beam jitter. Additionally, further PSP measurements will be performed over the entire surface of the turret, to ensure no important links are missed by only correlating with pressure fields on the downstream portion of the turret. Finally, an optimization study on optimal sensor locations can be performed with the goal of providing the largest possible reduction in the total beam jitter for an open loop control system using the LSE technique presented in this paper.

## References

- [1] S. Gordeyev and E. Jumper, “Fluid Dynamics and Aero-Optics of Turrets”, *Progress in Aerospace Sciences*, **46**, (2010), pp. 388-400.
- [2] C. Porter, S. Gordeyev, M. Zenk and E. Jumper, “Flight Measurements of the Aero-Optical Environment around a Flat-Windowed Turret”, *AIAA Journal*, Vol. **51**, No. 6, Jun. 2013, pp. 1394-1403.
- [3] N. De Lucca, S. Gordeyev and E.J. Jumper, “In-flight aero-optics of turrets”, *Journal of Optical Engineering*, **52**(7), 071405, 2013.
- [4] M. Wang, A. Mani and S. Gordeyev, “Physics and Computation of Aero-Optics”, *Annual Review of Fluid Mechanics*, Vol. **44**, pp. 299-321, 2012.
- [5] P.E. Morgan and M.R. Visbal., “Hybrid Reynolds-Averaged Navier-Stokes/Large-Eddy Simulation Investigating Control of Flow over a Turret”, *Journal of Aircraft*, **49**(6), pp. 1700-1717, 2012.
- [6] R. Jelic, S. Sherer and R.Greendyke, “Simulation of Various Turret Configurations at Subsonic and Transonic Flight Conditions Using OVERFLOW”, AIAA Paper 2012-464, 2012.
- [7] N. De Lucca, S. Gordeyev and E. Jumper, “The Study of Aero-Optical and Mechanical Jitter for Flat Window Turrets”, AIAA Paper 2012-0623.
- [8] K. Hird, T. J. Juliano, J. Gregory, N. Delucca, S. Gordeyev, E. Jumper, J. Thordahl and D.J. Wittich, “Study of Unsteady Surface Pressure on a Turret via Pressure-Sensitive Paint”, 44nd AIAA Plasmadynamics and Lasers Conference, 24-27 June 2013, San Diego, California, AIAA Paper 2013-3137.

- [9] S. Gordeyev, N. De Lucca, E. Jumper, K. Hird, T. J. Juliano, J. Gregory, J. Thordahl and D.J. Wittich, "Comparison of Unsteady Pressure Fields on Turrets with Different Surface Features using Pressure Sensitive Paint", to appear in *Experiments in Fluids*, 2014.
- [10] N. De Lucca, S. Gordeyev, E. Jumper, K. Hird, T. J. Juliano, J. Gregory, J. Thordahl and D.J. Wittich, "The Estimation of the Unsteady Force Applied to a Turret in Flight", 44th AIAA Plasmadynamics and Lasers Conference, 24-27 June 2013, San Diego, California, AIAA Paper 2013-3136.
- [11] S. Gordeyev, J.A. Cress, E. Jumper and A.B. Cain, "Aero-Optical Environment Around a Cylindrical Turret with a Flat Window", *AIAA Journal*, Vol. 49, No. 2, pp. 308-315, 2011.
- [12] Adrian, R.J., "On the role of conditional averages in turbulent theory", In: *Turbulence in Liquids: Proceedings of the 4th Biennial Symposium on Turbulence in Liquids*, ed. G. Pattersen and J. Zakin, Science Press, Princeton, 1977, pp. 322-33
- [13] G. Berkooz, P. Holmes, and J. Lumley, "The Proper Orthogonal Decomposition in the Analysis of Turbulent Flows", *Annual Review of Fluid Mechanics*, Vol. 25, No. 1, pp. 539-575, 1993.
- [14] N. De Lucca, S. Gordeyev, E. Jumper and D.J. Wittich, "Aero-Optical Environment around Turrets at Forward-Viewing Angles", AIAA Paper 2013-0721.
- [15] Whiteley, MR, Goorskey DJ, and Drye, R, "Aero-Optical Jitter Estimation Using Higher-Order Wavefronts", *Optical Engineering* 52(7), 071411 (July 2013)